Final Draft
of the original manuscript:

Ben-Hamu, G.; Eliezer, D.; Dietzel, W.; Shin, K.S.:
Stress Corrosion Cracking of new Mg-Zn-Mn wrought alloys containing Si
In: Corrosion Science (2008) Elsevier

DOI: 10.1016/j.corsci.2008.02.012

Stress Corrosion Cracking of new wrought Mg-Zn-Mn alloys containing S.

G. Ben-Hamu[a], D. Eliezer[a]*, W. Dietzel[b] and K. S. Shin[c]

[a] *Department of Materials Engineering, Ben-Gurion University of the Negev, PO Box 653, Beer-Sheva 84105, Israel*

[b] *Institute for Materials Research, GKSS-Forschungszentrum Geesthacht GmbH, D-21502 Geesthacht, Germany*

[c] *Magnesium Technology Innovation Center, School of Materials Science and Engineering, Seoul National University, 599 Gwanangno, Gwanak-gu Seoul 151-744, Korea*

∗ Corresponding author. *e-mail:* deliezer@bgu.ac.il

Tel.: +972-8-646-1467; Fax: +972-8-647-2931

Abstract

The stress corrosion cracking (SCC) of high strength and ductility Mg-Zn-Mn alloys containing Si was studied using the slow strain rate test (SSRT) technique in air and in 3.5 wt% NaCl solution saturated with $Mg(OH)_2$. All alloys were susceptible to SCC to some extent. The fractography was consistent with a significant component of intergranular SCC (IGSCC). The TGSCC fracture path in ZSM620 is consistent with a mechanism involving hydrogen. In each case, the IGSCC appeared to be associated with the second-phase particles along grain boundaries. For the IGSCC of the ZSM6X0 alloys, the fractography was consistent with micro-galvanic acceleration of the corrosion of α-magnesium by the second-phase particles, whereas it appeared that the second-phase particles themselves had corroded. The study suggests that Si addition to Mg-Zn-Mn alloys can significantly improve SCC resistance as observed in the case of ZSM620. However, the SCC resistance also depends on the other critical alloying elements such as zinc and the microstructure.

Keywords: Mg-Zn alloy; Stress corrosion cracking; Mg_2Si intermetallics

1. Introduction

The high susceptibility of Mg alloys to corrosion and stress corrosion limits their application in automotive and aerospace industries. However, the majority of growth has been in the area of die-cast components and some semi-solid formed components [1]. The corrosion behavior of Mg alloys has been extensively studied for different cast compositions (e.g., AZ31, AZ61 and AZ91) [2–7]. The introduction of these alloys enables extrusion of components for automotive and aerospace applications. These are often exposed to environments containing aggressive species such as chlorides that cause localized corrosion such as pitting and stress corrosion cracking (SCC) [8–14].

Wrought magnesium alloys represent approximately 1% of total magnesium consumption. There are two major technical issues related to expanding the wrought magnesium market. The first is the low production rate. A typical magnesium alloy must be extruded 5–10 times slower than a typical aluminum alloy. The second is the development of new wrought magnesium alloys with a combination of high strength, high ductility and high corrosion resistance.

In recent years, the modification of alloy composition and/or heat treatment has been attempted for improved mechanical properties [15] and corrosion resistance [16] in the casting alloys. However, there is a growing need for high strength wrought Mg alloys in the automotive and aerospace industries. Generally, four alloy systems have been utilized for the development of the wrought Mg alloys, i.e., Mg-Zn, Mg-Al, Mg-Th, and Mg-Mn alloys [17]. Among these, Mg-Zn alloys were found to have a large

age-hardening response, stemming from the precipitation of a transition phase (β'), and consequently offered a combination of good strength and ductility [18]. It has been reported, however, that is difficult to achieve grain refinement in Mg-Zn alloys [10]. Several alloying elements, including Zr, RE and Cu, have been added to Mg-Zn alloys to improve the mechanical properties; Zr for grain refining and strengthening [19,20], rare-earth (RE) for improved high temperature properties [20] and Cu for ductility improvement [21,22].

Literature on the SCC behavior of Zn-, Mn- and Si-containing magnesium alloys is limited. However, even the available literature reports contradictory views. Winzer et al.'s [11] review of the SCC behavior of magnesium alloys shows that elements such as neodymium, silver, zirconium, lithium, lead, copper, nickel, tin and thorium had little or no influence on SCC susceptibility. The addition of Zn has been reported to increase SCC susceptibility [23], although this was disputed by Fairman and Bary [24]. Mg-Zn alloys containing rare earths, such as the ZExx series of alloys, are generally considered to have moderate SCC susceptibility relative to Mg-Al-Zn alloys. M.B. Kannan reported that the transganular SCC (TGSCC) fracture in ZE41in distilled water was consistent with a mechanism involving hydrogen, whereas the intergranular SCC (IGSCC) in ZE41 in 0.5 wt% NaCl solution was associated with the second phase particles along grain boundaries [25].

Mg-Mn alloys have generally been considered to be immune to pitting in the atmosphere, chloride solutions and chloride-chromate solutions [23], but have also been reported to be susceptible to pitting in the atmosphere and in distilled water [26].

This tends to conflict with the commonly-proposed role of pitting in the initiation of stress corrosion. Chloride solutions generally promote pitting whilst distilled water promotes more uniform corrosion. In contrast to the general belief regarding SCC resistance of Mg-Mn alloys, Timonova et al. [26] showed SCC for Mg-Mn alloys in solutions containing chloride and sulfate ions, and Nozaki et al. [27] showed SCC for commercial Mg-2 % Mn-0.5 % Ce in distilled water and 0.5% potassium hydrogen fluoride solution. Timonova [28] stated that the addition of Mn or Zn to Mg-8 % A1 decreased susceptibility; however, the addition of both elements together was stated to increase susceptibility.

The influence of Si is not reported in the literature. The objective of this work is to characterize the SCC behavior of new wrought Mg-Zn-Mg alloys containing Si (ZSM600, ZSM610 and ZSM620) using the slow strain rate test method in chloride-containing solution. For comparison, the alloy not containing Si (ZM60) was also studied.

2. Experimental procedure

Mg-Zn alloys were melted in a low carbon steel crucible; the melt surface was protected with a gas mixture of CO_2+0.5% SF_6. Zn, with 99.99% purity, was added to the melt. Silicon was added to the melt in the form of Mg-10 wt% Si master alloy. The alloy designations used in the present study are listed in Table 1. The ingots were homogenized at 400°C for 48 hours, water-cooled, and subsequently scalped to give 77 mm diameter billets. After preheating, the billets were extruded at 300^0C with an extrusion ratio of 25:1 to give 16 mm diameter cylindrical rods.

Specimens for optical microscopy were mechanically polished followed by chemical etching with a 1% HNOs + 24% distilled water + 75% diethylene glycol solution.
All the samples were characterized in the as-extruded condition. The phases present in the Mg–6% Zn–0.5% Mn (ZSM) alloys were identified using a SEM microscope equipped with EDXS and XRD.

SCC susceptibility was studied using the slow strain rate test (SSRT) method. Round tensile specimens with gauge dimensions 22 mm (length) × 5 mm (diameter) were used. The tensile samples were ground with SiC paper up to 1200 grit and cleaned with acetone prior to testing. In the SSR tests, the tensile samples were tested at strain rates of 10−6 and 10−7 s−1 in air or 3.5 wt% NaCl solution saturated with $Mg(OH)_2$. For comparison, the mechanical properties were measured in air at a strain rate of 10−4 s−1 in a universal testing machine.

The SSRT machine maintained a constant strain rate by means of an open-loop control system; the average specimen elongation was measured by two linear variable displacement transducers (LVDTs) attached at opposite sides of the specimen fixtures in parallel with the specimen whilst a geared synchronous motor increased the elongation and thus the load accordingly. All values of strain rate given in this paper are nominal ones, based on the elongation measured by a pair of LVDTs. These measurements were used to control, in a feed-back circuit, the crosshead speed of the test machine, to achieve a constant rate of increase in displacement. Here, a uniform deformation over the entire gauge section of the specimen was assumed. The actual

strain and hence the actual strain rate at the site of failure, caused by either mechanical rupture or by SCC, could not be measured with the equipment used.

The SCC susceptibility was evaluated using the parameters elongation to failure (f) and ultimate tensile strength (UTS), both measured in an inert atmosphere (air) and in the corrosive environments. After the SSR tests, the fracture surfaces were examined using a scanning electron microscope (SEM).

3. Results

3.1. Microstructure

The microstructure of the as-extruded ZM60, ZSM600, ZSM610 and ZSM620 alloys is shown in Figure 1. The average grain sizes of the extruded ZSM alloys were 23 μm, 12.1 μm, 11.3 μm and 10.3μm, respectively. As shown in Figure 1, fine Mg_2Si phases are distributed parallel to the extrusion direction in the ZSM6X0 alloys. The type of Mg_2Si particles was polygonal script when the Si content was equal to or more than 1 wt% (Fig. 2 (b)). When the Si content was 0.5 wt%, the Mg_2Si particles were Chinese script type (Fig. 2 (a)). Therefore, the grain refinement of the Mg-Zn-Mn-Si alloy can be explained as grain growth that is suppressed by the formation of precipitates containing Mg and Si during recrystallization. The Mg_2Si polygonal particles are created by breaking of the Chinese script type Mg_2Si during the extrusion process. The polygonal script Mg_2Si phases are dispersed parallel to the extrusion direction in the as-extruded ZSM alloys.

The SEM micrographs in Figure 2 present the typical morphology of the intermetallic compounds identified in the extruded ZSM6X0 magnesium alloy, i.e., $MgZn_2$, Mn_5Si_3 and Mg_2Si. The $MgZn_2$ phase appears as clusters of small particles which are aligned in the extrusion direction. The latter morphology is probably caused by the extrusion process that fractures the intermetallic compounds. The Mn_5Si_3 intermetallics often have a polygonal shape. The microstructure of the alloys containing Si depends on the quantity of Si. Low Si content alloys (~ 0.5 wt%) exhibit Chinese script type Mg_2Si. However, Si content of more than 0.5 wt% changed the Mg_2Si to polygonal type.

In addition, XRD measurement was used in order to recognize the phase presented in the ZSM alloys containing different quantities of Si. In the spectrum taken from the alloy without silicon addition, weak peaks due to $MgZn_2$ and MgZn phases have been identified. As the silicon content of the alloy increases, the peak intensity for $MgZn_2$ and MgZn appears to decrease while that for Mg_2Si increases (Fig. 3).

3.2. Slow strain rate testing

The stress–strain curves of ZM60, ZSM600, ZSM610 and ZSM620 tested in air, and the apparent stress–strain curves in 3.5 wt% NaCl solution saturated with $Mg(OH)_2$ at strain rates of 10^{-6} and 10^{-7} s^{-1} are presented in Figure 4(a-d). Mechanical property data of the four alloys in air are presented in Table 2, which includes comparison data in air at a strain rate of 10^{-4} s^{-1}. The summary of SSRT data of the four alloys tested in air and in 3.5 wt% NaCl solution saturated with $Mg(OH)_2$ is shown in Table 3.

The mechanical property values measured in this study at a strain rate of 10^{-4} s^{-1} in air are consistent with data in the literature [29]. However, the strain to fracture values in air measured at a strain rate of 10^{-6} s^{-1} were significantly higher than those measured in air at a strain state of 10^{-4} s^{-1} (i.e., ε_f (10^{-6}) > ε_f (10^{-4})) for ZM60, ZSM600 and ZSM610, whereas ε_f (10^{-6}) < ε_f (10^{-4}) for ZSM620. This shows the ZSM6X0 alloys are very sensitive to strain rate.

ZM60 tested at a strain rate of 10^{-6} s^{-1} in air exhibited ε_f = 33% and UTS = 290 MPa (Fig. 5(a)). The mechanical properties were significantly lower when tested at a strain rate of 10^{-7} s^{-1}: ε_f = 2% and UTS = 120 MPa when tested in 3.5 wt% NaCl solution saturated with $Mg(OH)_2$ (Fig. 4(a) and Table 3).

ZSM600 when tested at a strain rate of 10^{-6} s^{-1} in air exhibited ε_f = 32% and UTS = 290 MPa (Fig. 5(b)). The mechanical properties were significantly lower when tested at a strain rate of 10^{-7} s^{-1}: ε_f = 2% and UTS = 130 MPa when tested in 3.5 wt% NaCl solution saturated with $Mg(OH)_2$ (Fig. 4(b) and Table 3).

ZSM610 when tested at a strain rate of 10^{-6} s^{-1} in air exhibited ε_f = 27% and UTS = 315 MPa (Fig. 5(c)). The mechanical properties were significantly lower when tested at a strain rate of 10^{-7} s^{-1}: ε_f = 2.5% and UTS = 175 MPa when tested in 3.5 wt% NaCl solution saturated with $Mg(OH)_2$ (Fig. 4(c) and Table 3).

ZSM620 when tested at a strain rate of 10^{-6} s^{-1} in air exhibited ε_f = 15% and UTS = 310 MPa (Fig. 5(d)). The mechanical properties were significantly lower when tested

at a strain rate of 10^{-7} s^{-1}: ε_f = 3% and UTS = 200 MPa when tested in 3.5 wt% NaCl solution saturated with $Mg(OH)_2$ (Fig. 4(d) and Table 3).

3.3. Macrographs

A stereomicroscope was used to obtain the macrographs of fractured SSRT samples of all the ZSM6X0 alloys after the tests in air and in 3.5 wt% NaCl solution saturated with $Mg(OH)_2$ (Fig. 5 (a–h)). In air, as the Si content increased more secondary cracks were observed throughout the gauge length (arrow in Fig. 5(a-d)). In the corrosive environment, the ZM60 showed significant localized corrosion and general corrosion; a few fine stress corrosion cracks throughout the gauge length were observed (Fig. 5(e)). ZSM600 showed more localized corrosion in comparison with ZM60. However, ZSM600 did not undergo larger number of cracks then ZM60 (Fig. 5(f)). ZSM610 exhibited significant localized corrosion (Fig. 5(g)), as did ZSM620 (Fig. 5(h)). The density of the stress corrosion cracks increased as the Si content increased. High pit density was observed in ZSM620. The fracture mechanics differed in the alloys depending on the quantity of Si. In the alloys without Si content, the fracture mode was flat and in the alloys with Si the fractures were angled. ZSM620 with high Si content had a very high angle mode in comparison with the alloys with low Si content.

3.4. Fractography

Typical fracture surfaces of ZSM6X0 alloys after SSRT in air at strain rate of 10^{-6} s^{-1} are shown in Figure 6(a–d). The fracture surfaces of ZM60 (Fig. 6(a)) and ZSM600 (Fig. 6(b)) in air show ductile features. The fracture surfaces of ZSM610 (Fig. 6(c)) and ZSM620 (Fig. 6(d)) (in air) show mixed-mode fractures having features associated with both dimple rupture and brittle fracture of second-phase particles. Furthermore, ductile fracture was observed in the Mg matrix (for all ZSM6X0 alloys),

but the fracture preferentially occurred along the interface between the Mg_2Si particles and the Mg matrix.

The fracture surface of ZM60 in 3.5 wt% NaCl solution saturated with $Mg(OH)_2$ is shown in Figure 7(a-c). The fracture mode was of an intergranular nature. Many features were consistent with the appearance of corrosion along grain boundaries. There were features consistent with corrosion of α-phase leaving behind the second-phase particles. The fractography was consistent with a mixed intergranular and transgranular mode with intergranular failure being predominant (Fig. 7(c)). The α-phase that was visible had an appearance consistent with having been corroded (Fig. 7(b)).

The fracture surface of ZSM600 in 3.5 wt% NaCl solution saturated with $Mg(OH)_2$ is shown in Figure 8(a-b). The fracture mode was of a mixed intergranular and transgranular nature. Many features were consistent with the appearance of corrosion along grain boundaries. Other features were consistent with the corrosion of the grain on both sides of second-phase particles extending a considerable distance along several grain boundaries.

The fracture surface of ZSM610 in 3.5 wt% NaCl solution saturated with $Mg(OH)_2$ is shown in Figure 9(a-b). There is a generally smooth and undulated appearance, consistent with corrosion along the grain boundaries accelerated by micro-galvanic corrosion of second-phase particles that formed a nearly continuous necklace along the grain boundaries (Fig. 9(b)). The grain boundary surfaces themselves appeared as

if they had been chemically polished. There were isolated incidences of grain boundary attack into the plane of the fracture. Furthermore, the fracture surface revealed predominant brittle failure consistent with dissolution of the grain boundary precipitates. There were also some isolated areas that could be consistent with transgranular brittle fracture.

The fracture surface of ZSM620 in 3.5 wt% NaCl solution saturated with $Mg(OH)_2$ is shown in Figure 10(a-d). The circumferential edge of the fracture surface revealed significant pitting corrosion (Fig. 10(a)). Furthermore, transgranular parallel cracking is observed in this figure. A combined process of brittle fracture, corrosion and dimple rupture is shown in Figure 10(b-c). The fracture mode was intergranular in nature mixed with isolated transgranular. Many features were consistent with the appearance of corrosion along grain boundaries. There were features consistent with corrosion of α-phase leaving behind the second-phase particles, also with features consistent with the brittle fracture of the second-phase particles (Fig. 10(d)).

3.5 Secondary Cracking

Secondary cracks were apparent on the gauge surfaces of ZM60, ZSM600, ZSM610 and ZSM620 specimens fractured in 3.5 wt% NaCl solution saturated with $Mg(OH)_2$ (Figures 11–14).

The density of secondary cracks in ZM60 was considerably less in comparison to the alloys containing Si. In ZM60 and ZSM600 the secondary cracks were normal to the loading direction and were macroscopically sharp and propagating intergranular in a

relatively constant direction (Figures 11 and 12, respectively) direction. However, for ZSM610 and ZSM620 secondary cracks were observed perpendicular to the load direction. These secondary cracks were nucleating within the polygonal type Mg_2Si (Figures 13(b) and 14(b), respectively). This is consistent with the brittle nature of the Mg_2Si intermetallics. Those secondary cracks originated from the brittle Mg_2Si and extended to voids in the bulk of the samples. In case of secondary cracks that were observed in a normal to the loading direction, the cracks cross the grain boundaries (intergranular SCC); however the crack's tip was near the Mg_2Si polygonal type. The polygonal type Mg_2Si acts as a barrier for stress corrosion crack propagation (Figures 13(a) and 14(a)). The thicknesses of the secondary cracks differed as the Si content increased. The thickness of ZSM600 was the larger (65 μm) in comparison to ZSM610 (28 μm) and ZSM620 (16 μm). This difference is explained due to the different corrosion behavior of the ZSM6X0 alloys [31].

4. Discussion

In order to quantify the SCC susceptibility of the alloys, the SCC susceptibility indices (I_{SCC}) were calculated based on a particular mechanical property value measured in an SSRT test in a corrosive environment compared to its corresponding value in an inert environment. In this study, 3.5 wt% NaCl solution saturated with $Mg(OH)_2$ was considered a corrosive environment and air as an inert environment. In order to quantify the chloride-induced SCC, the ratio between the mechanical properties in 3.5 wt% NaCl solution saturated with $Mg(OH)_2$/Air was calculated. A low I_{SCC} index corresponds to high SCC susceptibility; when the I_{SCC} index

approaches unity this means that there is no effect due to the test environment or that the alloy is highly resistant to SCC in the particular test environment.

The SCC susceptibility indices for ZSM6X0 alloys obtained at 10^{-6} and 10^{-7} s^{-1} strain rates are presented in Table 4. ZM60 showed a higher SCC susceptibility in 3.5 wt% NaCl solution saturated with $Mg(OH)_2$ than the same alloy containing different quantities of Si (0.5, 1 and 2 wt%). The SCC susceptibility indices were low (~0.06) for ZM60. ZSM620 showed higher SCC resistance than ZSM610, ZSM600 and ZM60. In general, the SCC susceptibility indices for ZSM6X0 alloys were very low in comparison to the ZE41 (containing 4 wt% Zn) alloy reported by Kannan et al. [25]. Assuming that I_{SCC} (3.5 wt% NaCl solution saturated with $Mg(OH)_2$/Air) corresponds to chloride-induced SCC, the following points can be made. The chloride-induced SCC was much higher for the alloys containing less Si. ZSM620 also showed slightly higher chloride-induced SCC.

The macrographs of the fractured SSRT samples showed that the alloys alloying with Si had undergone relatively higher general and localized corrosion than ZM60. ZM60 showed better general corrosion resistance; however, high localized corrosion occurred preferentially along the interface of $MgZn_2$ and Mn_5Si_3 due to a galvanic effect [30]. However, the localized corrosion was observed in all the studied alloys due to $MgZn_2$ intermetallics that distributed as small dots at the grain boundaries (Fig. 2(b)). These intermetallics have very high electrochemical potential related to the magnesium matrix [30]. Inclusion of $MgZn_2$ in the magnesium alloys increased the

micro-galvanic sites on the surface and also increased the localized corrosion attack near the grain boundaries.

The fracture modes of all four alloys tested in air and 3.5 wt% NaCl solution saturated with $Mg(OH)_2$ are given in Table 5. In air, all the alloys failed in transgranular mode; ZM60 with a ductile fracture – as the Si content increased in the Mg-Zn-Mn alloy the fracture mode changed to features associated with both dimple rupture and brittle fracture. The fracture preferentially occurred along the interface between the Mg_2Si particles and the Mg matrix. In a 3.5 wt% NaCl solution saturated with $Mg(OH)_2$, ZM60 predominantly failed in IGSCC mode; the alloys containing Si showed a mixed mode of failure, i.e., IGSCC and TGSCC, that was dependent on the Mg_2Si type. ZSM600 (0.5 wt% Si) has Chinese script type Mg_2Si; from our earlier [31] corrosion study on this system this type of Mg_2Si intermetallic increased the dissolution of α phase. However, when Si content increased to 1 wt% or more, polygonal type Mg_2Si was form. Alloys containing polygonal type Mg_2Si exhibit high corrosion resistance in comparison to the alloys with Chinese script type Mg_2Si. During the stress corrosion test, the dissolution of the grain (α phase) was much higher in ZSM600 in comparison to ZSM610 and ZSM620. Due to this in case of ZSM600 TGSCC and IGSCC were observed. Furthermore, the Si content influenced the grain size. The alloys containing high Si content exhibit lower grain size. Many authors have stated that magnesium and its alloys mostly undergo TGSCC. Others claim that IGSCC is dominant for certain metallurgical conditions. In this study, it is seen that the fine-grained ZSM620 underwent TGSCC and the relatively larger grains in ZSM610 and ZSM600 underwent mixed-mode failure, i.e., IGSCC and TGSCC, and ZM60

underwent IGSCC. This observation is not full in agreement with Stampella et al. [32] who reported that the crack morphology was determined by the grain size and that for fine-grained magnesium SCC was exclusively transgranular, whereas for larger grained magnesium SCC was mixed transgranular and intergranular. IGSCC is continuous and completely electrochemical; TGSCC is discontinuous and involves alternating mechanical and electrochemical processes, as reported by Pardue et al. [33]. In fact, TGSCC is mostly related to hydrogen-induced cracking [34, 35]. Stampella et al. [32] suggested that atomic hydrogen in a solid solution of magnesium facilitates cleavage fracture. Based on the fracture surface analysis in this study, it is suggested that the fracture path observed in ZSM6X0 in 3.5 wt% NaCl solution saturated with $Mg(OH)_2$ is consistent with a mechanism involving hydrogen. Especially in ZSM620, the fracture surface analysis observed parallel cracking related to mechanism involving hydrogen. The IGSCC appeared in chloride-containing solution to be associated with corrosion induced by the second-phase particles. For ZSM6X0 alloys the fractography was consistent with micro-galvanic acceleration of the corrosion of α-magnesium by the second-phase particles, whereas it appeared that the second-phase particles had themselves corroded in the case of ZSM600 in chloride containing solution.

5. Conclusions

The SCC tendency of the four Mg-Zn-Mn alloys under test can be summarized as follows, based on the SSRT in air and 3.5 wt% NaCl solution saturated with $Mg(OH)_2$:

1. ZSM6X0 alloy was susceptible to SCC in the corrosion solution to some extent. ZSM620 (with 2 wt% Si) had the highest resistance to SCC.
2. The transgranular SCC (TGSCC) fracture in ZSM620 was consistent with a mechanism involving hydrogen, whereas, the intergranular SCC (IGSCC) in the studied alloys was associated with the second-phase particles along grain boundaries ($MgZn_2$).
3. Fine-grained ZSM620 exhibited more areas with TGSCC, in comparison to the other ZSM6X0 alloys that were coarser grained.
4. Two secondary cracks were observed in ZSM610 and ZSM620 – perpendicular and parallel to the load direction. The perpendicular secondary cracks originated from the brittle Mg_2Si and propagated to voids in the bulk of the samples. In the case of secondary cracks that were observed normal to the loading direction, the cracks cross the grain boundaries (intergranular SCC); however, the crack's tip was near the Mg_2Si polygonal type.
5. The study suggests that Si addition in Mg-Zn-Mn alloys can improve SCC resistance significantly as observed in the case of ZSM620. However, the SCC resistance also depends on the other critical alloying elements, for example, the presence of zinc.
6. The SCC susceptibility indices for ZSM6X0 alloys were very low in comparison to the alloys reported by Kannan et al. [25].

References

[1] C.D. Yim, K.S. Shin, Mater. Trans. 44(4) (2003) 558.

[2] M. Avedesian, H. Baker, Magnesium and Magnesium Alloys, ASM International, Materials Park, 1998.

[3] D. Eliezer, P. Uzan, E. Aghion, Mater. Sci. Forum 419–422 (2003) 857.

[4] S. Mathieu, C. Rapin, J. Steinmetz, P. Steinmetz, Corros. Sci. 45 (2003) 2741.

[5] R.K. Singh Raman, Metall. Mater. Trans. A 35 (2004) 2525.

[6] Y.J. Ko, C.D. Yim, J.D. Lim, K.S. Shin, Mater. Sci. Forum 419–422 (2003) 851.

[7] G. Song, A.L. Bowles, D.H. St. John, Mater. Sci. Eng. A366 (2004) 74.

[8] G.L. Song, A. Atrens, Adv. Eng. Mater. 1 (1999) 11.

[9] G.L. Song, A. Atrens, Adv. Eng. Mater. 5 (2003) 837.

[10] E. Ghali, W. Dietzel, K.U. Kainer, J. Mater. Eng. Perform. 13 (2004) 7.

[11] N. Winzer, A. Atrens, G. Song, E. Ghali, W. Dietzel, K.U. Kainer, N. Hort, C. Blawert, Adv. Eng. Mater. 7 (2005) 659.

[12] M. Bobby Kannan, W. Dietzel, C. Blawert, S. Riekehr, M. Kocak, Mater. Sci. Eng. A 444 (2007) 220.

[13] M. Bobby Kannan, W. Dietzel, R. Zeng, J.F. dos Santos, R. Zettler, Mater. Sci. Eng. A 460–461 (2007) 243.

[14] M. Bobby Kannan, W. Dietzel, R.K. Singh Raman, P. Lyon, Scr. Mater. 57 (2007) 579.

[15] D.H. Kim, SJ. Song, H. Park, K.S. Shin, Met. Mater. 3 (1997) 51.

[16] C.D. Lee, C.S. Kang, K.S. Shin: Met. Mater. 6 (2000) 351.

[17] C.S. Roberts, Magnesium and Its Alloys, John Wiley & Sons, Inc., New York, 1960.

[18] L. Sturkey, J.B. Clark, J. Inst. Met. 88 (1959-60) 177.

[19] A.K. Bhambri, T.Z. Kattamis, Metall. Trans. 2 (1971) 1869.

[20] T.E. Leontis, Trans. AIME, 180 (1949) 287.

[21] W. Unsworth, J.F. King, Magnesium Technology, The Institute of Metal, city, 1987, p. 25.

[22] E.A. Ball, P.B. Prangnell, Scripta Metall. et Mater. 31 (1994) 111.

[23] W.K. Miller, in: Stress Corrosion Cracking: Materials Performance and Evaluation, ASM International, USA 192, p. 251.

[24] L. Fairman, H.J. Bary, Corrosion Science 11 (1971) 533.

[25] M. Bobby Kannan, W. Dietzel, C. Blawert, A. Atrens, P. Lyon, Materials Science and Engineering A, (2007) Article in Press.

[26] M.A Timonova, Intercrystalline Corrosion and Corrosion of Metals Under Stress, Ed. I.A. Levin, Great Britain, 1962, 251.

[27] T. Nozaki, S. Hanaki, M. Yamashita, H. Uchida, Proceedings of the 13th Asian Pacific Corrosion Control Conference, Osaka, Japan, 2003, K-15.

[28] M.A. Timonova, Intercrystalline Corrosion and corrosion of metals under stress, Ed. I.A. Levin, Great Britain, 1962, 263.

[29] J.H Hwang, D. Eliezer, K.S Shin, Proc. of the 1st Asian Symposium on Magnesium Alloys, B.S. You, K.S. Shin, S. Kamado, W. Ding (Eds.), Jeju, Korea, 2005, pp. 117-120.

[30] G. Ben-Hamu, D. Eliezer, K.S. Shin, Materials Science and Engineering A 447(1-2) (2007) 35-43.

[31] G. Ben Hamu, D. Eliezer, K.S. Shin, Proc. of the Corrosion Control 007, Mohammad Ali (Ed.), Sydney, Australia, 2007.

[32] R.S. Stampella, R.P.M. Procter, V. Ashworth, Corros. Sci. 24 (1984) 325.

[33] W.M. Pardue, F.H. Beck, M.G. Fontana, Trans. Am. Soc. Met. 54 (1961) 539.

[34] A. Atrens, N. Winzer, G.L. Song, W. Dietzel, C. Blawert, Adv. Eng. Mater. 8 (2006) 749.

[35] N. Winzer, A. Atrens, W. Dietzel, G. Song, K.U. Kainer, Mater. Sci. Eng. A 466 (2007) 18.

Table 1. Chemical Composition of the wrought ZSM6X0 Mg alloys (wt%).

Alloy	Zn	Mn	Si	Fe (max)	Ni (max)	Cu (max)
ZM60	6	0.5	–	0.04	0.005	0.05
ZSM600	6	0.5	0.5	0.04	0.005	0.05
ZSM610	6	0.5	1.0	0.04	0.005	0.05
ZSM620	6	0.5	2.0	0.04	0.005	0.05

Table 2: Mechanical properties of the ZSM6*X*0 alloys.

Alloy	Strain rate, s^{-1}	$\varepsilon_{f,\%}$	0.2% proof stress, MPa	UTS, MPa
ZM60	Typical	17	206	280
	10^{-6}	33	160	290
ZSM600	Typical	18	187	285
	10^{-6}	32	155	290
ZSM610	Typical	19	191	314
	10^{-6}	27	185	315
ZSM620	Typical	20	70	300
	10^{-6}	15	195	310

Table 3: Summary of SSRT results of ZSM6*X*0 alloys.

Alloy	Strain rate, s^{-1}	$\varepsilon_{f,\%}$		UTS, MPa	
		Air	NaCl+$Mg(OH)_2$	Air	NaCl+$Mg(OH)_2$
ZM60	10^{-6}	33	-	290	-
	10^{-7}	-	2	-	120
ZSM600	10^{-6}	32	-	290	-
	10^{-7}	-	2	-	130
ZSM610	10^{-6}	27	-	315	-
	10^{-7}	-	2.5	-	175
ZSM620	10^{-6}	15	-	310	-
	10^{-7}	-	3	-	200

Table 4: The I_{SCC} susceptibility indices for ZSM6*X*0.

Alloy	I_{SCC} (NaCl/air)	
	ε_f	UTS
ZM60	0.06	0.41
ZSM600	0.06	0.45
ZSM610	0.09	0.55
ZSM620	0.2	0.65

Table 5: Fracture modes of ZSM6*X*0 in air and NaCl solution.

Alloy	Fracture modes	
	Air	NaCl
ZM60	Transgranular-ductile fracture	IGSCC/TGSCC
ZSM600	Transgranular-ductile fracture	IGSCC/TGSCC
ZSM610	Transgranular cleavage fracture and a few fine dimples	IGSCC/TGSCC
ZSM620	Transgranular-dimple rupture and brittle fracture	IGSCC/TGSCC

TGSCC: transgranular stress corrosion cracking, IGSCC: intergranular stress corrosion cracking.

Figure Legends

Figure 1. Typical microstructure of extruded ZM60 (a), ZSM600 (b), ZSM610 (c), and ZSM620 (d) alloys by optical microscopy.

Figure 2. SEM micrographs of the microstructure of ZSM600 (a) and ZSM620 (b) alloys.

Figure 3. XRD pattern from ZSM6X0 alloys.

Figure 4. Stress–strain plot of: (a) ZM60, (b) ZSM600, (c) ZSM610 and (d) ZSM620 tested in air and 3.5 wt% NaCl solution saturated with $Mg(OH)_2$.

Figure 5. Macrographs of failed SSRT samples in air: (a) ZM60, (b) ZSM600, (c) ZSM610 and (d) ZSM620; in 3.5 wt% NaCl solution saturated with $Mg(OH)_2$: (e) ZM60, (f) ZSM600, (g) ZSM610 and (h) ZSM620.

Figure 6. SEM micrographs of specimen fractured in air; ZM60 (a), ZSM600 (b) ZSM610 (c) and ZSM620 (d).

Figure 7. SEM micrographs of ZM60 fractured surface in 3.5 wt% NaCl solution saturated with $Mg(OH)_2$ (a); intergranular and transgranular (arrow) cracking (b).

Figure 8. SEM micrographs of ZSM600 fractured surface in 3.5 wt% NaCl solution saturated with $Mg(OH)_2$ (a); predominant intergranular and isolated transgranular (arrow) cracking (b).

Figure 9. SEM micrographs of ZSM610 fractured surface in 3.5 wt% NaCl solution saturated with $Mg(OH)_2$ (a); predominant intergranular and isolated transgranular (arrow) cracking (b); intergranular cracking (arrow) (c).

Figure 10. SEM micrographs of ZSM620 fractured surface with transgranular parallel cracking in 3.5 wt% NaCl solution saturated with $Mg(OH)_2$ (a); transgranular

cracking and few fine dimples (arrow) (b); localized corrosion (c); intergranular cracking and second phase particles (arrow) (d).

Figure 11. Optical microscopy of secondary crack for ZM60.

Figure 12. Optical microscopy of secondary crack for ZSM600.

Figure 13. Optical microscopy of secondary crack for ZSM610; secondary crack perpendicular to the load direction (a), secondary crack parallel to the load direction (b).

Figure 14. Optical microscopy of secondary crack for ZSM620; secondary crack perpendicular to the load direction (a), secondary crack parallel to the load direction (b).

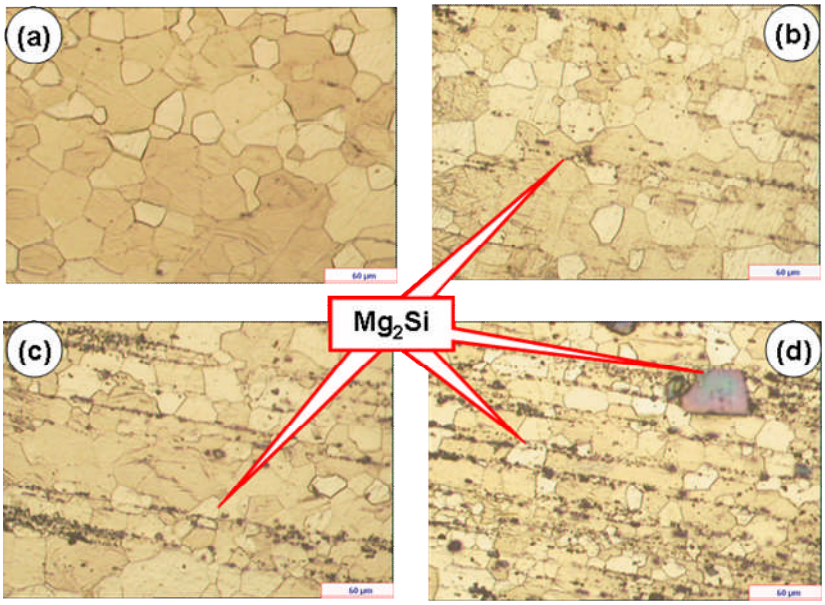

Figure 1.

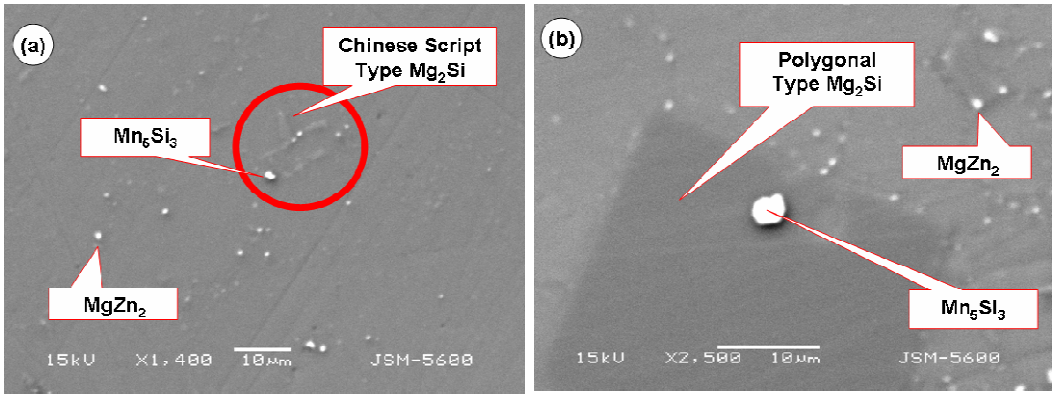
(a)
Chinese Script
Type Mg2Si
Mn6Si3
MgZn2
15kV X1,400 10μm JSM-5600
(b)
Polygonal
Type Mg2Si
MgZn2
Mn5Si3
15kV X2,500 10μm JSM-5600

Figure 2.

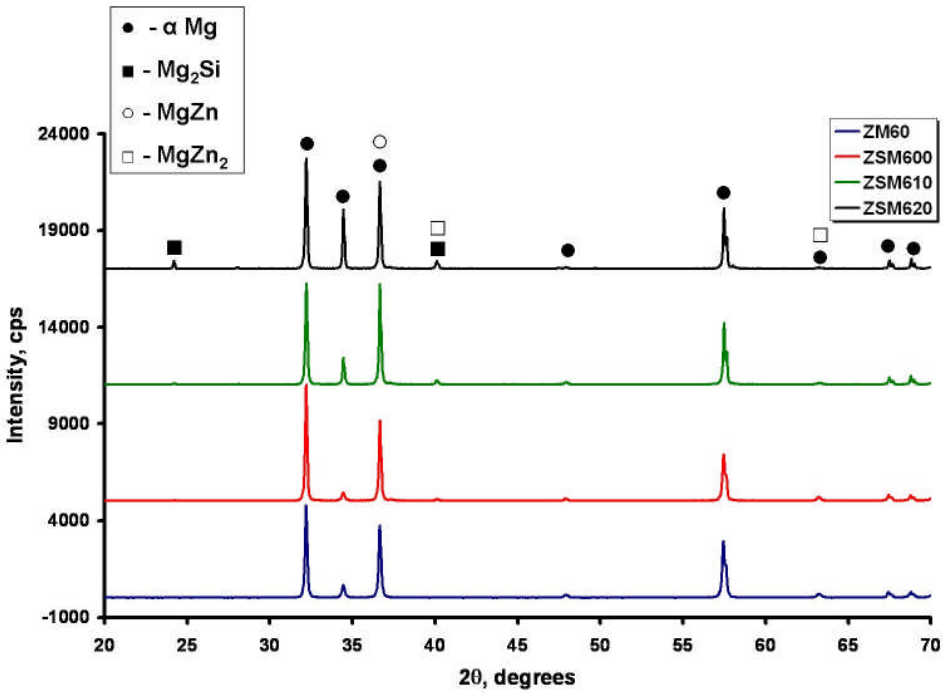
● - α Mg
■ - Mg2Si
○ - MgZn
□ - MgZn2
ZM60
ZSM600
ZSM610
ZSM620
Intensity, cps
24000
19000
14000
9000
4000
-1000
20
25
30
35
40
45
50
55
60
65
70
2θ, degrees

Figure 3.

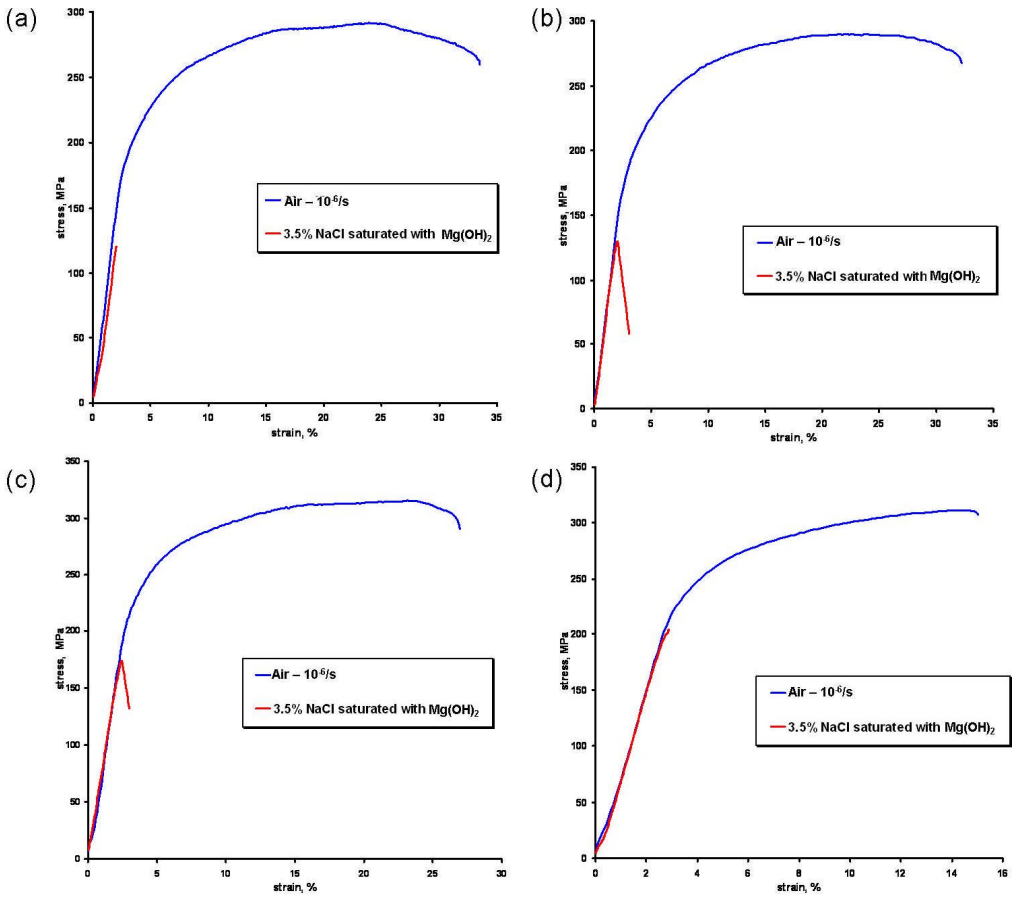
(a)
stress, MPa
strain, %
Air – 10⁻⁶/s
3.5% NaCl saturated with Mg(OH)2
(b)
stress, MPa
strain, %
Air – 10⁻⁶/s
3.5% NaCl saturated with Mg(OH)2
(c)
stress, MPa
strain, %
Air – 10⁻⁶/s
3.5% NaCl saturated with Mg(OH)2
(d)
stress, MPa
strain, %
Air – 10⁻⁶/s
3.5% NaCl saturated with Mg(OH)2

Figure 4.

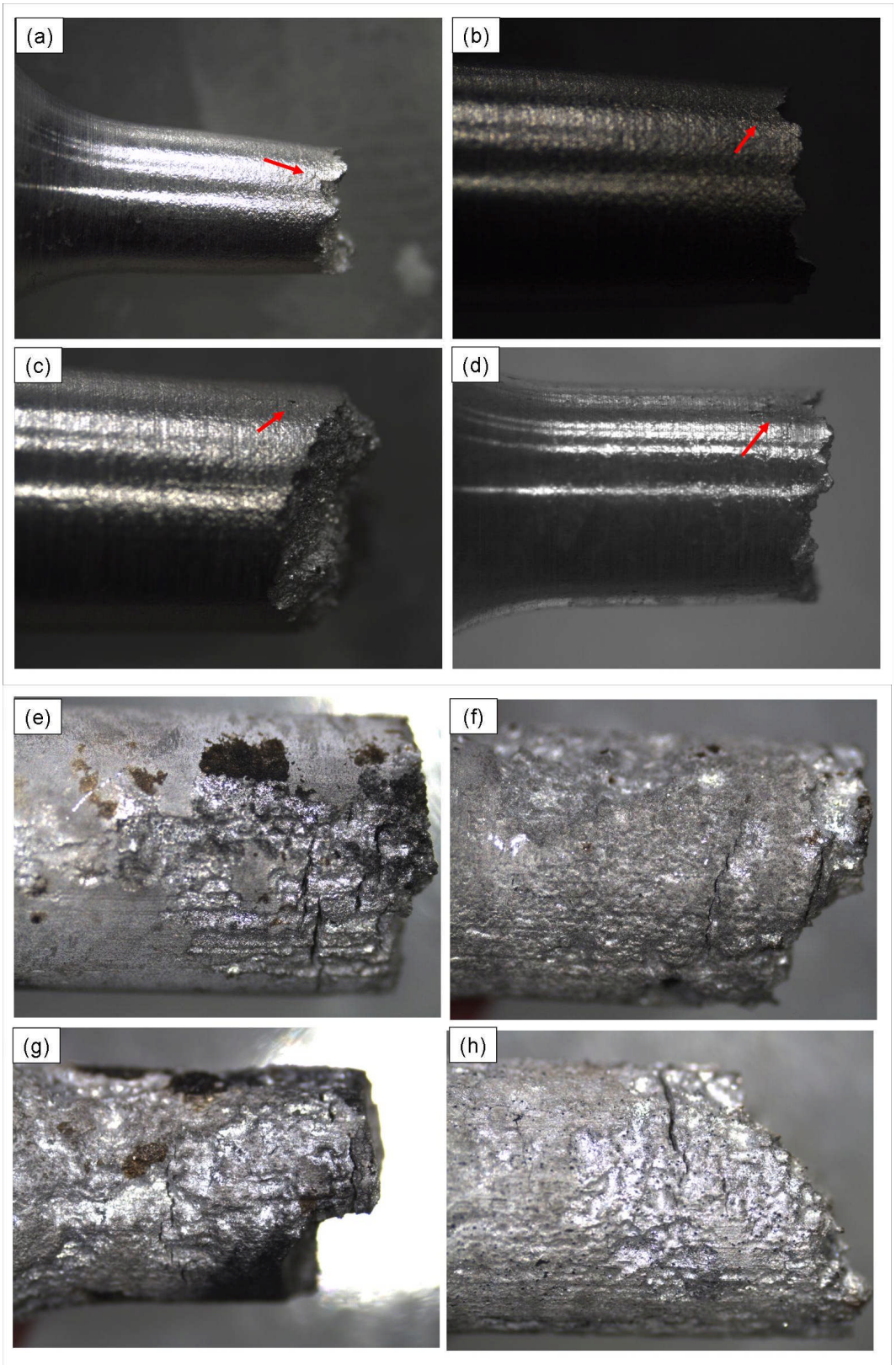

Figure 5.

.

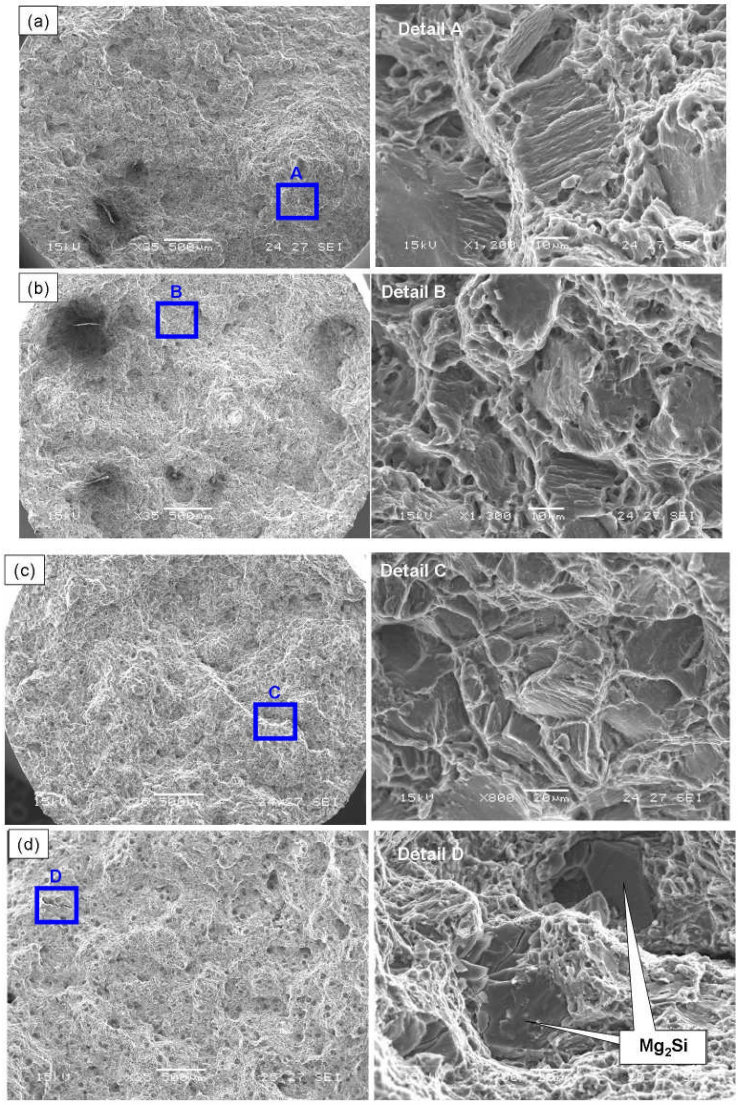

Figure 6.

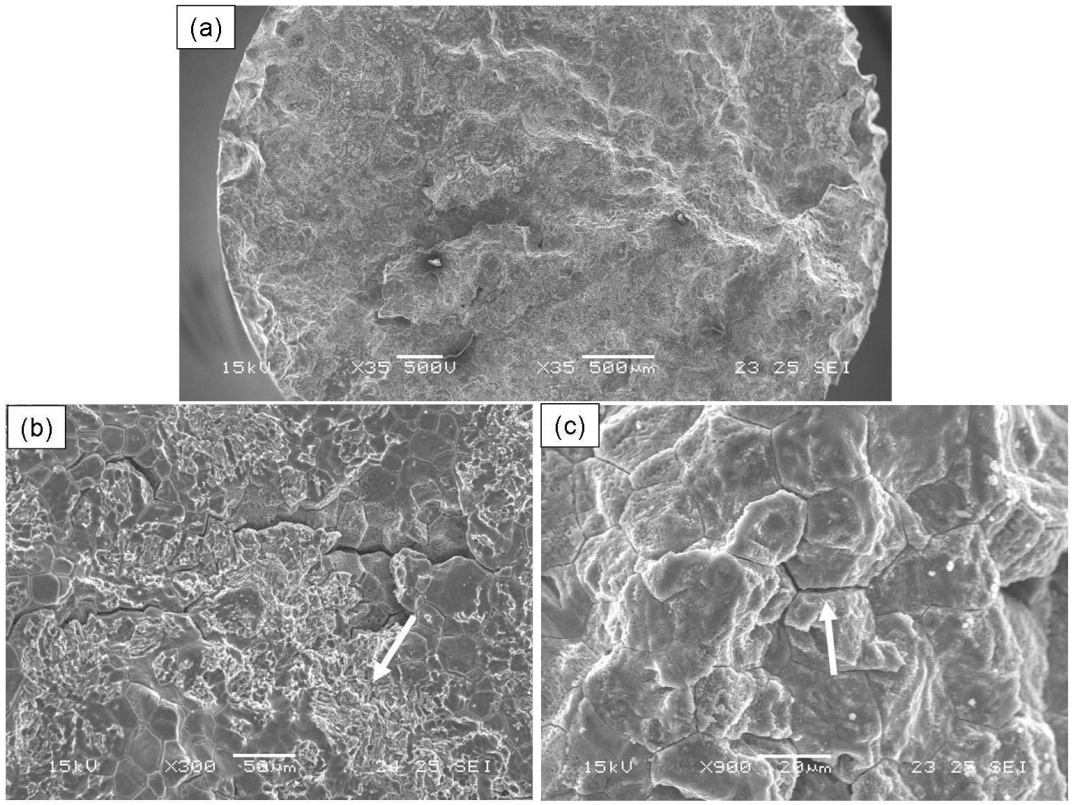
(a)
15kV X35 500V X35 500µm 23 25 SEI
(b)
15kV X300 50µm 24 25 SEI
(c)
15kV X900 20µm 23 25 SEI

Figure 7.

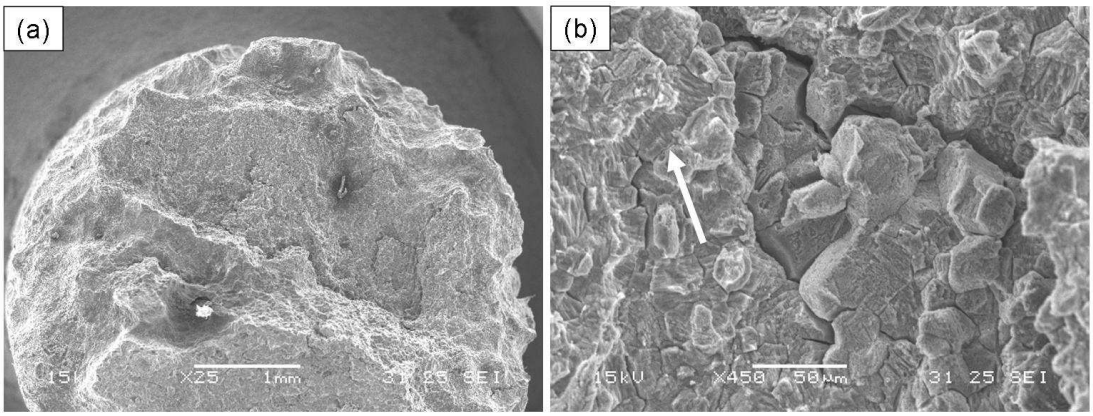

Figure 8.

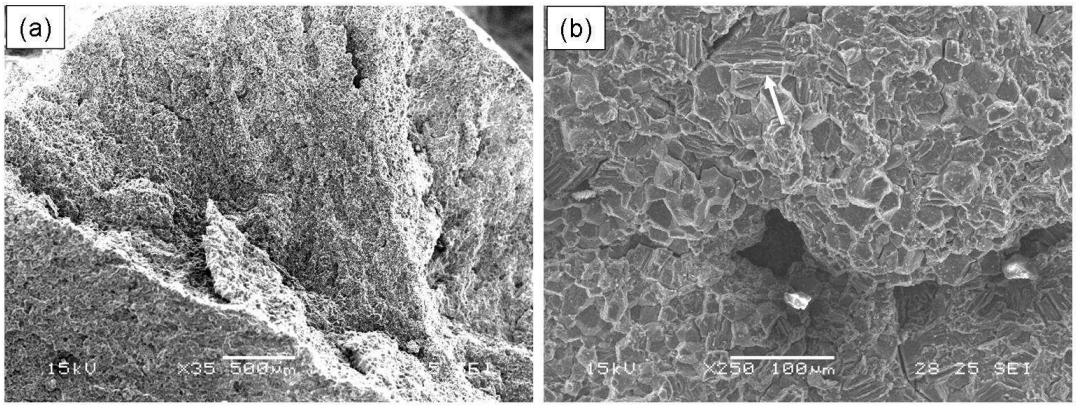

Figure 9.

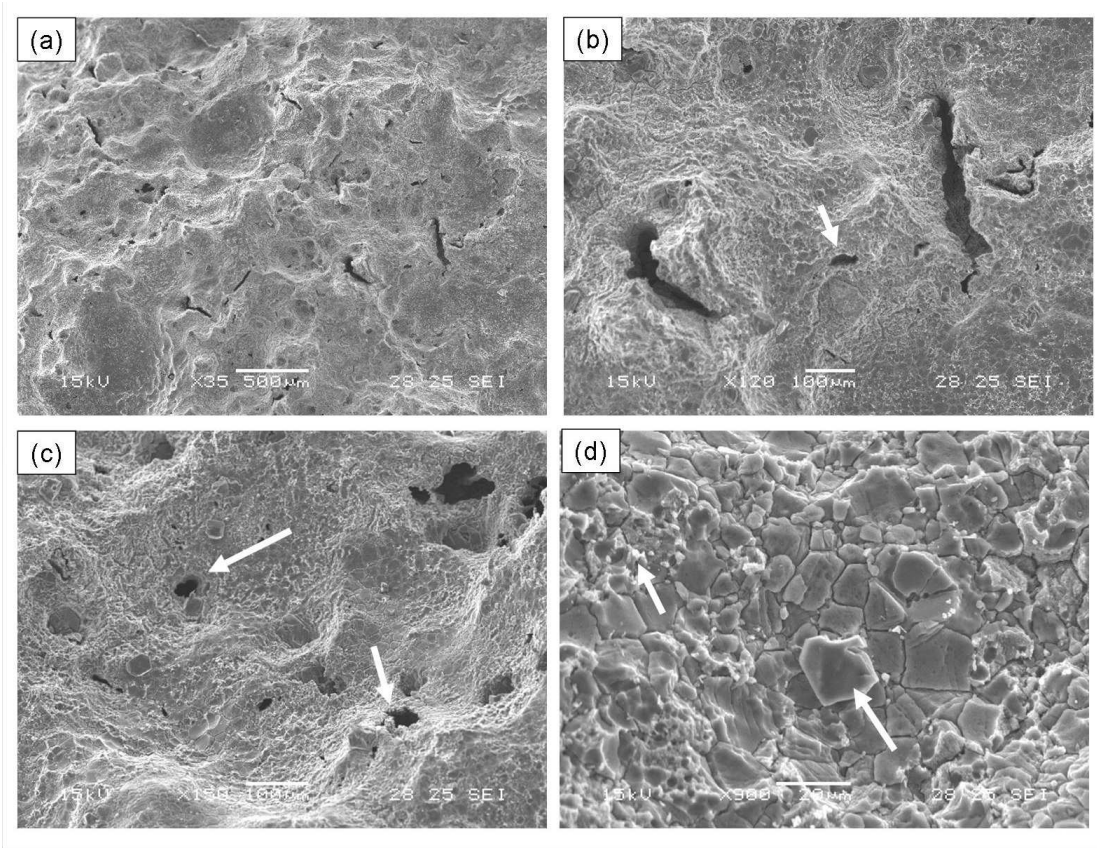

Figure 10.

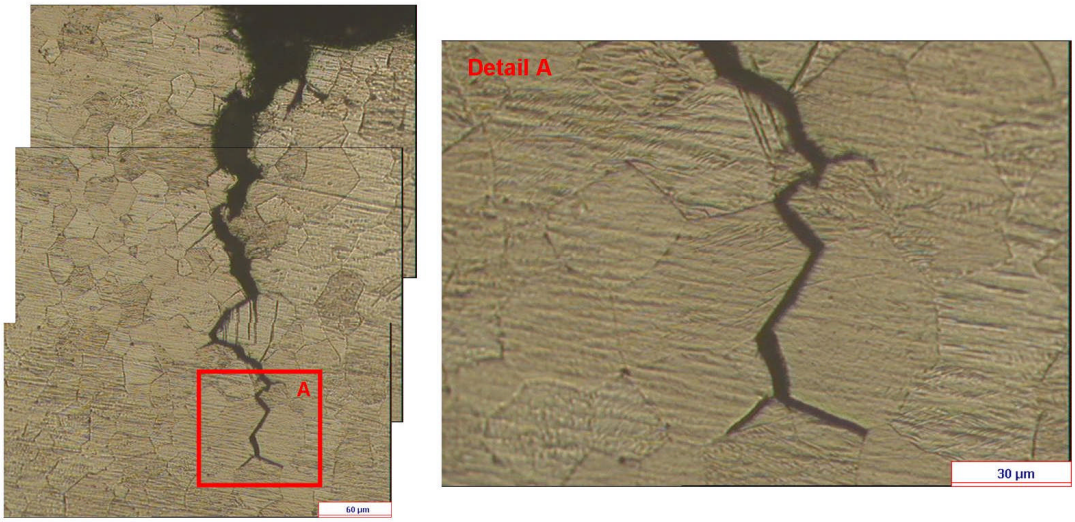

Figure 11.

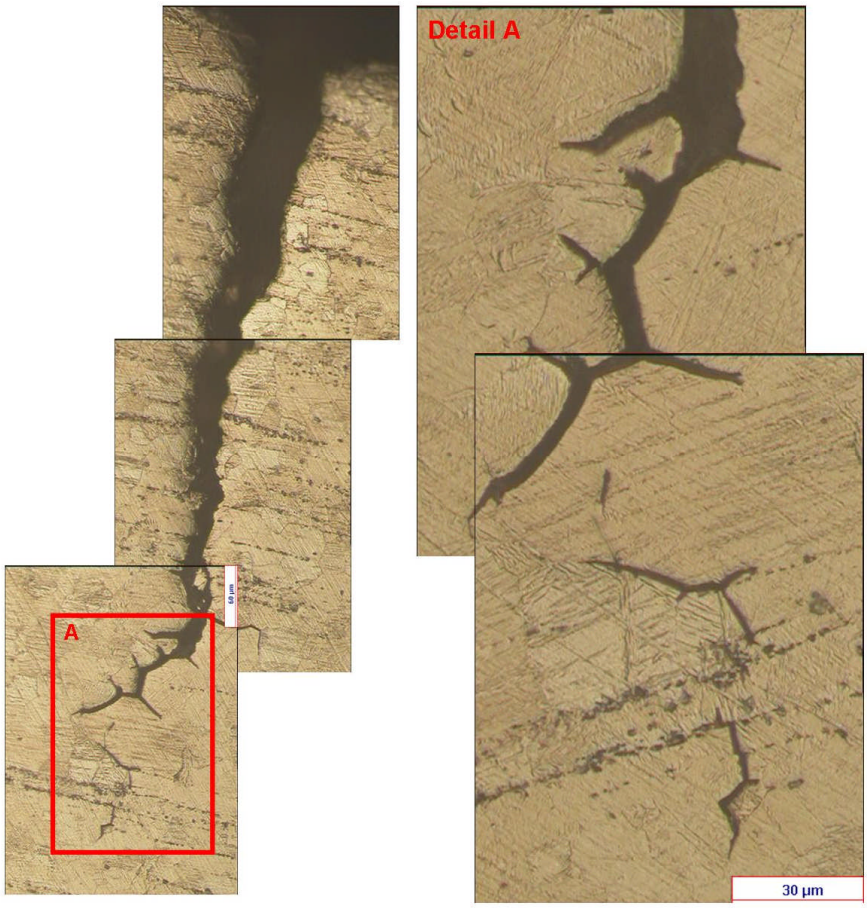

Figure 12.

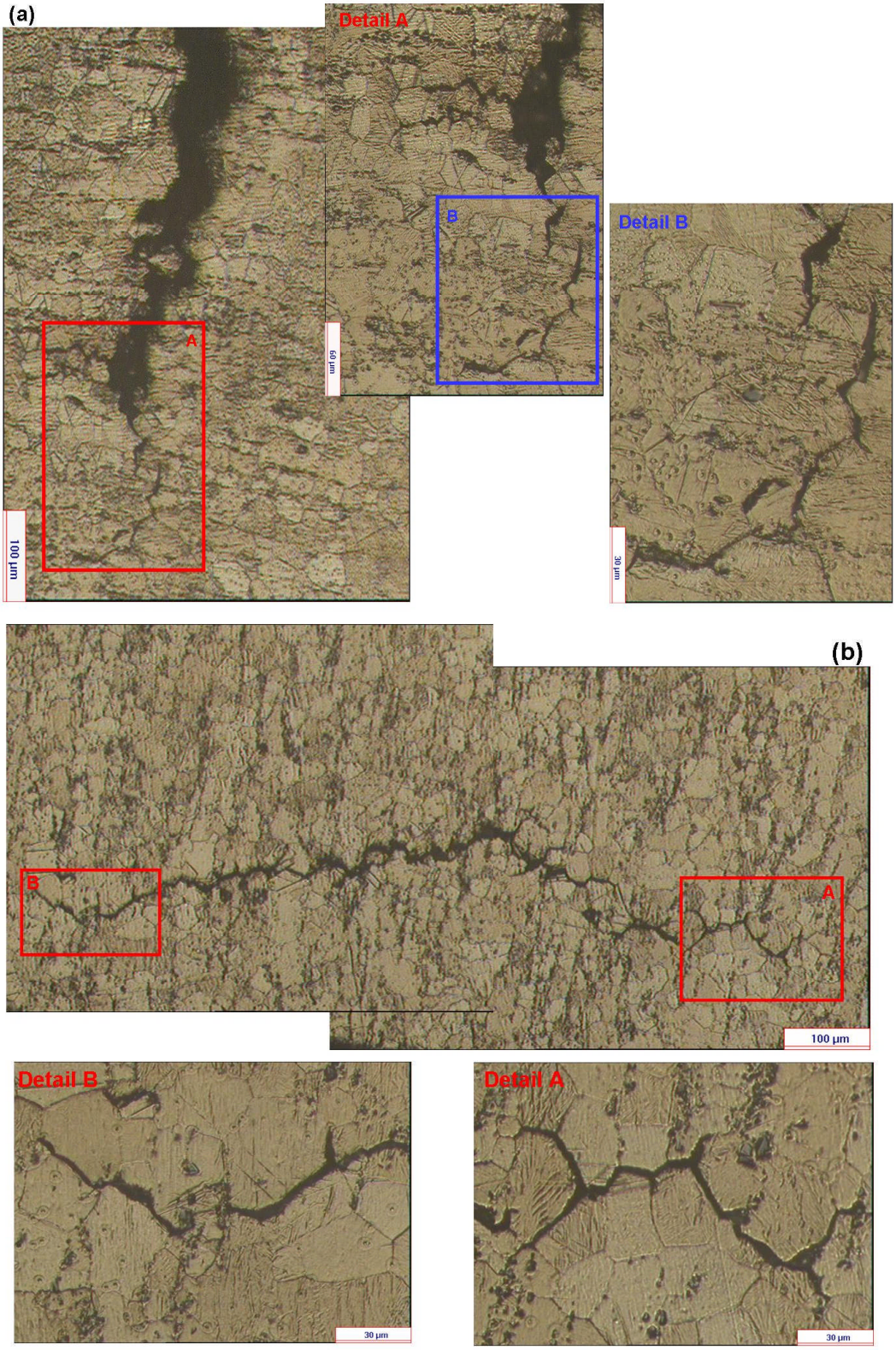
(a)
Detail A
B
Detail B
A
100 µm
60 µm
30 µm
(b)
B
A
100 µm
Detail B
Detail A
30 µm
30 µm

Figure 13.

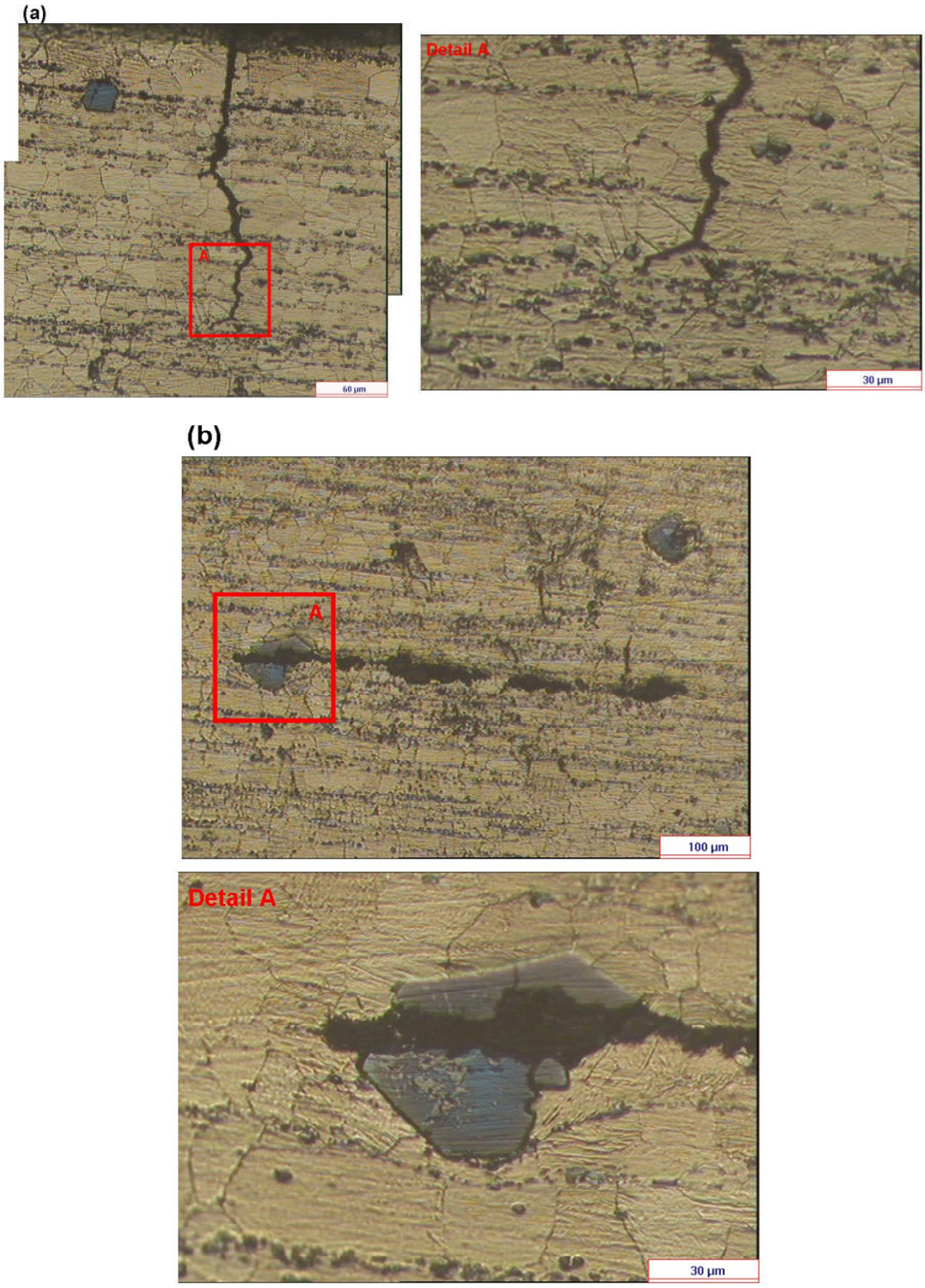

Figure 14.